Letter

Reconstruction of moiré lattices in twisted transition metal dichalcogenide bilayers

Indrajit Maity, Prabal K. Maiti, H. R. Krishnamurthy, and Manish Jain*
Centre for Condensed Matter Theory, Department of Physics, Indian Institute of Science, Bangalore-560012, India

(Received 23 January 2020; accepted 17 February 2021; published 1 March 2021)

An important step in understanding the exotic electronic, vibrational, and optical properties of the moiré lattices is the inclusion of the effects of structural relaxation of the unrelaxed moiré lattices. Here, we propose novel structures for twisted bilayer of transition metal dichalcogenides. For $\theta \gtrsim 58.4^\circ$, we show a dramatic reconstruction of the moiré lattices, leading to a trimerization of the unfavorable stackings. We show that the development of curved domain walls due to the threefold symmetry of the stacking energy landscape is responsible for such lattice reconstruction. Furthermore, we show that the lattice reconstruction notably changes the electronic band structure. This includes the occurrence of flat bands near the edges of the conduction as well as valence bands, with the valence band maximum, in particular, corresponding to localized states enclosed by the trimer. We also find possibilities for other complicated, entropy stabilized, lattice reconstructed structures.

DOI: 10.1103/PhysRevB.103.L121102

The formation of flat bands in the electronic band structure of moiré patterns of two-dimensional materials is central to understanding the observed exotic electronic phases [1–4]. Twisted bilayer transition metal dichalcogenides (tBLTMDs) can possess flat bands for a continuum of twist angles [5–15]. To accurately calculate their electronic band structure, incorporation of structural relaxation effects is crucial [5,6,16–21]. Typically, these relaxations are performed by starting from a configuration and *only* allowing downhill motion in the potential energy landscape using local search algorithms (standard minimization). Since the number of local minima in the potential energy landscape increases exponentially with the number of atoms, standard minimizations are often insufficient for finding the stable structures [22–24]. All the studies conducted on moiré materials to date presume that the moiré lattice constant of the unrelaxed twisted structure remains intact even after relaxation. [1–10,16–20,25–28].

Here, from the structures obtained using simulated annealing (SA), we demonstrate that a dramatic reconstruction of moiré lattices of TMDs takes place for $\theta \gtrsim 58.4^\circ$. Thus, the presumption that the moiré lattice constant of the rigidly twisted structures continues to characterize the relaxed structures is not always valid. Such lattice reconstructions are not accessible in standard minimization approaches. We use the term lattice reconstruction restrictively, only in contexts where the lattice constant of the relaxed moiré lattice is different from the unrelaxed moiré lattice. We discuss below the details of the lattice reconstruction for tBL of MoS_2. We have also verified our conclusions for $MoSe_2$, WSe_2, WS_2 (see Supplemental Material, Sec. II [29]). We demonstrate that the lattice reconstruction substantially changes the electronic band structure.

We use the TWISTER code [5] to construct tBLTMDs. We relax the tBLTMDs in LAMMPS using standard minimization [30,31], denoted as standard relaxation (SR). We also perform classical molecular dynamics simulations using the canonical ensemble at $T = 1$ K, cool down snapshots to 0 K, and then carry out an energy minimization. We refer to this second approach as SA. We use the Stillinger-Weber and Kolmogorov-Crespi (KC) potential to capture the intralayer and interlayer interaction of tBLTMDs, respectively [32,33]. The used KC parameters have been shown to accurately capture the interlayer van der Waals interaction present in the TMDs [33]. The phonon frequencies are calculated using modified PHONOPY [34] code. We perform electronic structure calculations using density functional theory [35] with SIESTA [36–43] (see Supplemental Material, Sec. I for details [29]).

Due to the presence of different sublattice atoms (Mo/W, S/Se) in TMD, the tBLTMD possesses distinct high-symmetry stackings for θ near 0° (AA, AB, BA) and near 60° (AA′, AB′, A′B) [44]. Nevertheless, the lattice constants of the unrelaxed tBL are identical for θ and $60^\circ - \theta$ (e.g., 1° and 59°). Among the above-mentioned stackings, AB is energetically the most favorable stacking as $\theta \to 0^\circ$ ($E_{AB} = E_{BA} < E_{AA}$, sixfold symmetric around AA) and AA′ for $\theta \to 60^\circ$ ($E_{AA'} < E_{AB'} < E_{A'B}$, threefold symmetric around A′B) [25,33].

In Fig. 1 we show the interlayer separation (ILS) landscape for a $3 \times 3 \times 1$ moiré supercell of $tBLMoS_2$, obtained using both SR and SA. The landscape for $\theta = 1^\circ$ is a representative of $\theta \to 0^\circ$ [Fig. 1(a), top panel]. With SR we find straight domain walls separating AB, BA stackings. On the other hand, the ILS landscape computed with SA shows a slight curling of the domain walls (DW) near AA stacking [Fig. 1(a), bottom panel]. Although the number of clockwise and counterclockwise curlings are equal, they do not always form a checkerboardlike pattern. While the checkerboard pattern is the lowest in energy, the energy difference between the checkerboard pattern and a random distribution of curlings is

*mjain@iisc.ac.in

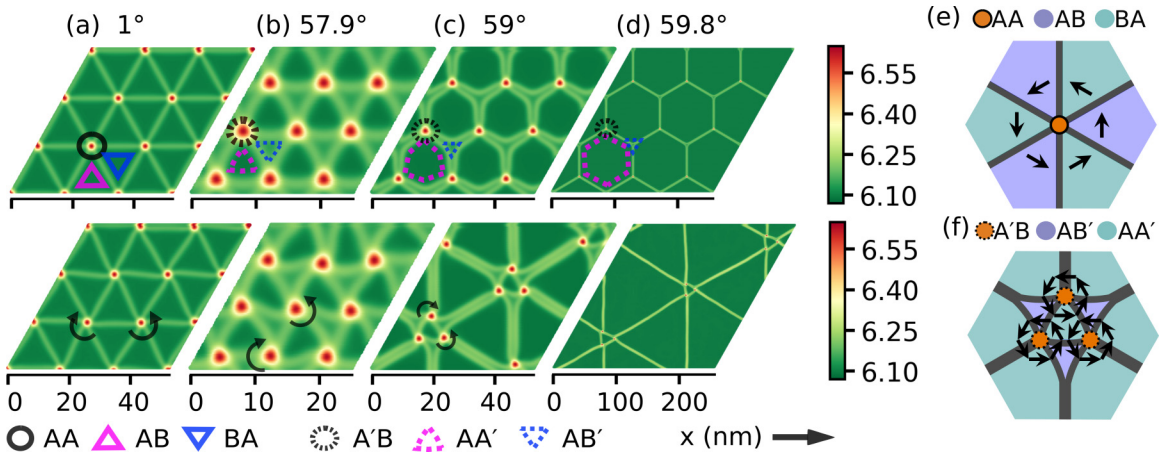

FIG. 1. (a)–(d): Interlayer separation landscape of $tBLMoS_2$ using SR (top panel) and SA (bottom panel). The smallest repetitive cell in the top panel is a moiré unit cell. The scales of the color bar are in Å and correspond to interlayer separation. The curling of DWs near a few AA, A′B stackings are marked. (e), (f): Schematics near the topological defects for tBLTMDs for $\theta = 1^\circ,\ 59^\circ$, respectively. The order parameter is shown with arrows.

small (a few meV per moiré lattice). Nevertheless, the AA stackings always form a triangular lattice for any θ close to 0°, consistent with experiments [9,27,28].

In contrast, the behavior of the ILS landscape shows very different and intriguing features as $\theta \to 60^\circ$. We categorize the θ dependence into two regions. Region I ($\theta < 58.3^\circ$): With SR both the AA′ and the AB′ stackings occupy comparable areas of the supercell, with each forming an approximate equilateral triangle [Fig. 1(b)]. Similar to $\theta \to 0^\circ$, the ILS landscape obtained with SA shows curlings of DWs near A′B stacking [Fig. 1(b), bottom panel]. Region II ($\theta \gtrsim 58.4^\circ$): The most favorable (AA′) stacking increases in area significantly and evolves from Reuleaux triangles to approximate hexagonal structures, as obtained with SR [Figs. 1(c) and 1(d), top panel], consistent with previous studies [25,26]. In this case, the DWs connecting A′B stackings are significantly curved and never straight lines. These latter structures *show notable reconstruction with SA*. In particular, a triangular lattice is formed with three A′B stackings trimerizing to form a motif [Figs. 1(c) and 1(d), bottom panel). Moreover, the DWs connecting different A′B stackings are almost straight in the reconstructed structures. The reconstructed structures obtained using SA are always energetically more stable than those obtained using SR.

We characterize the DWs using the order parameter, defined as the shortest displacement vector required to take any stacking to the most unfavorable stacking [5,16,45]. Irrespective of θ, we find the DWs to be shear solitons (change in order parameter is along the DW as we go from AB → BA for $\theta \to 0^\circ$ to AA′ → AA′ for $\theta \to 60^\circ$). In Region II, two DWs come close together and the effective width increases. For $\theta \to 0^\circ$ ($\theta \to 60^\circ$), the calculated widths of the DWs are : 2.9 (4.3) for $tBLMoS_2$, 2.9 (3.8) for $tBLMoSe_2$, 3.7 (4.7) for $tBLWSe_2$, and 3.5 (4.5) for $tBLWS_2$(all in nm). Our estimated DW widths are in good agreement with the experiment [27]. Moreover, the order parameter rotates by 2π at AA/A′B, indicating it's topological nature [Figs. 1(e) and 1(f)]. We do not find any new creation or annihilation of the topological defects and DWs in our simulations.

We investigate the structural long-range order by computing the radial distribution function. In the tBL there are two distinct length scales, one for the individual TMD layer given by the lattice constant a and the other for the moiré lattice given by the θ dependent moiré lattice constant, $a_m = a/[2\sin(\theta/2)]$. Therefore, we define two separate radial distribution functions, one for atoms of the individual layers and another for stackings of the moiré lattice. We compute the moiré-scale radial distribution function, $g_m(r)$ using the AA/A′B stackings of $tBLMoS_2$ [Fig. 2(a)]. Each AA/A′B stacking represents a moiré lattice point (MLP).

For $\theta \to 0^\circ$, $g_m(r)$ obtained using SR and SA are similar [Fig. 2(a)]. The average number of nearest neighbor MLPs is always 6, calculated by integrating the first peak of $g_m(r)$. This confirms the existence of the hexagonal network formed by DWs [Fig. 1(a)]. Furthermore, the moiré lattice constant calculated from $g_m(r)$ is identical to that of unrelaxed $tBLMoS_2$. Therefore, the long-range order of the unrelaxed structures remains intact as $\theta \to 0^\circ$. As $\theta \to 60^\circ$

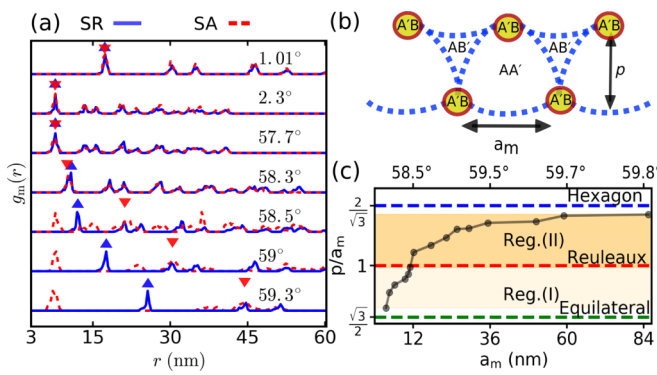

FIG. 2. (a) Radial distribution function, $g_m(r)$ computed with SR and SA. The moiré lattice constants are marked (blue triangle pointing up for SR, red triangle pointing down for SA). (b) Schematics of $tBLMoS_2$ as $\theta \to 60^\circ$ with SR. (c) Change of p/a_m with a_m. Several ideal geometric structures are marked with dashed lines.

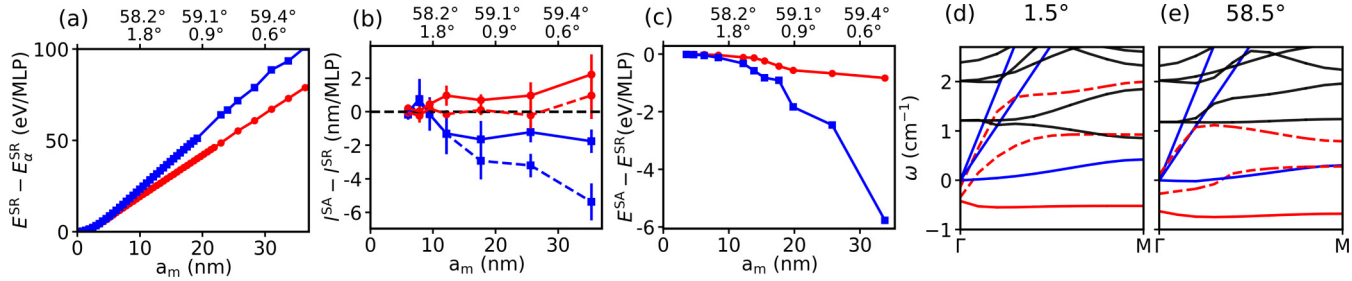

FIG. 3. (a) Change of total energy computed with respect to stable stacking, α using SR with a_m [corresponding θ are marked; blue (red) for near 60° (0°) for (a)–(c)]. (b) Change in DW length with SA compared to SR excluding (dashed lines) and including (solid lines) curling near AA/A′B. The error bar denotes SD of the estimated change. (d) Total energy gain with SA compared to SR. (d), (e) Phonon dispersion with SR for $1 \times 1 \times 1$ moiré cell. The solid blue, dashed red, solid red lines represent the acoustic, phason, buckling mode localized at AA/A′B, respectively.

within Region I, the moiré lattice constants are again identical for unrelaxed and relaxed structures, $a_m = a_m^{SR} = a_m^{SA}$ [Fig. 2(a)], and the number of nearest neighbor MLP is always 6. In contrast, the lattice reconstruction in Region II leads to the formation of a triangular lattice with a modified lattice constant, $a_m^{SA} = \sqrt{3}a_m$ [Fig. 2(a)]. The first peak in the $g_m(r)$ ($\approx$7.5 nm) corresponds to the motif of the triangular lattice. The motif consists of 3 A′B stackings. We find that the number of the nearest neighbor of A′B is 2. We also examine the atomic radial distribution function for individual MoS_2 layers. Irrespective of θ, the long-range order is preserved at the unit-cell MoS_2 scale. This establishes that the aforementioned reconstruction in Region II is an emergent phenomenon arising at the moiré scale.

To pinpoint the onset of the lattice reconstruction geometrically, we consider the ratio of the perpendicular bisector, p, to a_m of tBLMoS$_2$ obtained using SR [Fig. 2(b)]. Interestingly, we find lattice reconstruction as p/a_m becomes $\gtrsim 1$ [Fig. 2(c)]. When $p/a_m = 1$ ($\theta \sim 58.5°$), the AA′ stacking represents a Reuleaux triangle with the DWs occupying its perimeter. When one considers the perimeter^2 to area ratio, the Reuleaux triangle is a local maximum [46]. Since the DWs are energetically unfavorable compared to AA′, the Reuleaux triangle is expected to undergo rearrangements to minimize the total energy. The shortest distance between two A′B stackings is $\approx d^{A'B} + d^{AB'} \approx 3.3 + 4.5 = 7.8$ nm, where $d^{A'B}, d^{AB'}$ denote the sizes of the corresponding stackings. This explains the occurrence of first peak in $g_m(r)$ in Region II at $\approx$7.5 nm.

Next, we investigate the origin of these reconstructions from energetics. The total energy of the tBLMoS$_2$ is a sum of the intralayer energy, which is a combination of strain and bending energy [47], and the interlayer energy. For $\theta \to 60°$, the interlayer energy per MLP can be approximated as,

$$E_{inter} - E_{inter}^{AA'} = \delta E_{inter}^{A'B} S^{A'B} + \delta E_{inter}^{DW} S^{DW} + \delta E_{inter}^{AB'} S^{AB'}. \quad (1)$$

Here, $\delta E_{inter}^{\alpha}$ represents the interlayer energy of stacking α, evaluated with respect to AA′ and S^{α} denotes the occupied area. For small θ, $S^{A'B}$, $S^{AB'}$, and the width of the domain wall (DW), w, become constant ($S^{DW} = wl$). Therefore, the interlayer energy as in Eq.(1) becomes linear with the DW length, l, and is repulsive. Moreover, the intralayer strain energies are concentrated on the DWs and scales as l/w [45,48]. Thus, the minimization of l will minimize both the interlayer and the intralayer energies. In Fig. 3(a) we show the scaling of the total energy with a_m using SR. The DWs obtained with SR are always significantly curved for $\theta > 58.4°$. The lengths of these curved DWs can be minimized by lattice reconstruction such that the DWs become straightlines [as in Figs. 1(c) and 1(d), bottom panel]. On the other hand, the DWs are straightlines for the corresponding set of θ near 0° with SR. Thus, l per moiré lattice is already minimized. As a result, we do not find lattice reconstruction with SA as $\theta \to 0°$. However, the DWs obtained with SA are always curled near the AA, A′B stackings, irrespective of lattice reconstruction. This originates from a buckling instability, primarily localized at AA, A′B (see below). Taking these into account, l^{SA} is expected to be greater than l^{SR} in the absence of lattice reconstruction. In Fig. 3(b), we show the estimate of ($l^{SA} - l^{SR}$) per MLP as $\theta \to 0°$, $\to 60°$ (see Supplemental Material, Sec. III for details). For $\theta \gtrsim 58.4°$, the difference becomes negative, indicating a reduction in the DW length for the reconstructed lattice. The reduction in l, disregarding the curling of the DWs with SA, is large in Region II [Fig. 3(b)]. Figure 3(c) shows the gain in total energy with SA relative to SR, which is significantly greater in Region II than that for a corresponding θ near 0°. The energy gain near 0° arises from curling of the DWs near AA, whereas the gain in Region II arises predominantly from lattice reconstruction.

We also compare the low-frequency vibrational modes of 1.5° and 58.5° tBLMoS$_2$. One of the phason modes [49] softens significantly and becomes nearly dispersionless with attributes of a *zero* mode for 58.5° [Figs. 3(d) and 3(e)]. Such a mode is expected to cause reconstruction of lattices [50]. Furthermore, with SR we find a soft mode with imaginary frequency for both 1.5° and 58.5° [Figs. 3(d) and 3(e)]. The corresponding eigenvector at Γ, which is localized on AA/A′B, denotes a buckling instability and can be removed without lattice reconstruction.

During our simulations we find transient structures, such as distorted hexagon, kagome, etc, which evolve to form the structures shown in Figs. 1(c) and 1(d) (Supplemental Material, Sec. IV). To investigate entropic effects, we also simulate a supercell with 100 moiré lattices allowing significantly large degrees of freedom for lattice reconstruction. We find that lattice reconstructed structures with motifs of >3A′B stackings, nonuniform hexagons with parallel DWs, are also possible (Supplemental Material, Sec. IV). These structures

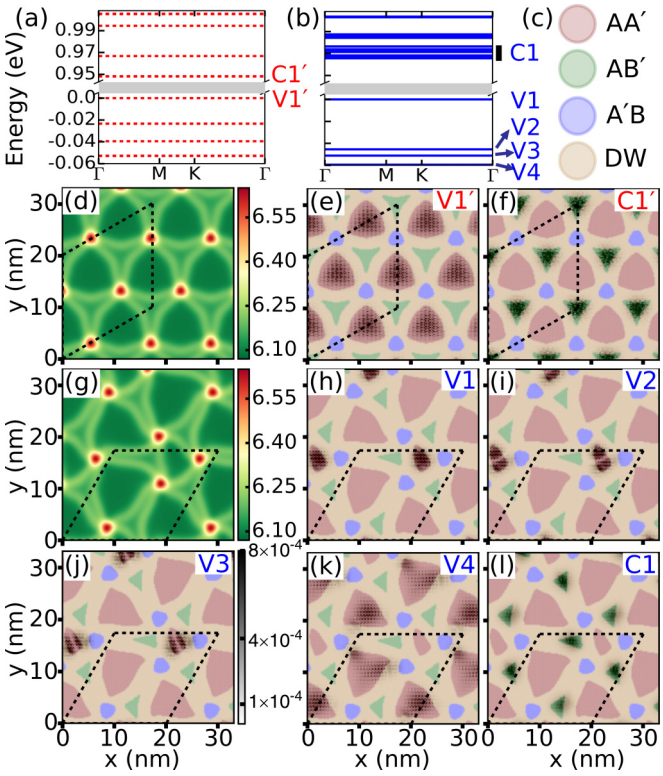

FIG. 4. (a) and (b) Electronic band structures near the band edges of a $\sqrt{3} \times \sqrt{3} \times 1$ supercell of $tBLMoS_2$ for 58.47° with SR and SA, respectively. The supercell is marked with black dashed lines. (c) Colors used to denote stackings in (e), (f), (h), and (l). (d) and (g) ILS landscape for 58.47° with SR and SA, respectively. $|\psi_\Gamma(\vec{r})|^2$ averaged in the out-of-plane direction of the states near VBM, and near CBM for structures obtained with SR [(e) and (f)] and with SA [(h) and (l)] with the corresponding color bar shown in (j). A linear combination is shown in (l) as C1 corresponding to bands marked in (b).

can be metastable due to the presence of a substrate, strain, etc. in an experiment. These external effects can modify the characteristic angle for the onset of lattice reconstruction. Our study suggests that the highly nonuniform hexagons with complex DW structures found in the experiments [27,28] are closely connected to the intrinsic lattice reconstruction. The "breathing" of hexagons in a hexagonal network of DWs can give rise to distorted hexagons and carry large entropy [51]. Our calculations suggest that these effects are realized for a general class of DW networks in moiré materials (Reuleaux triangle to hexagons).

In Figs. 4(a) and 4(b) we compare the electronic band structures of $tBLMoS_2$ obtained for 58.47°, which contains 24,966 atoms. The lattice reconstruction leads to an increment in the band-gap by ∼20 meV and significant changes in the spacing of energy levels near the band edges. Interestingly, we find the bands are ultraflat (bandwidth $\lesssim$1 meV within DFT) near the band edges for both the structures obtained with SR and SA. However, the wave-function localizations corresponding to these flat bands are strikingly different. To illustrate this, we show the density associated with the first few bands near the band edges. With SR, the states near the valence band maximum (VBM) resemble the states of a particle confined in a two-dimensional equilateral triangular well and are localized on AA′ [Figs. 4(c) and 4(e)] [6]. In the reconstructed lattice, the degeneracies associated with the equilateral triangular well are lifted, as triangles of various shapes and depths are realized. In particular, the wave functions corresponding to the first three bands near the VBM are localized on the AA′ stacking enclosed by the trimer [Figs. 4(h) and 4(j)], whereas for the fourth band, the wave function is localized on the larger AA′ stackings [Fig. 4(k)]. Since the area enclosed by the trimer in the reconstructed lattice [Fig. 4(g)] is θ independent, the spatial extension of the localized VBM is expected to be θ independent. The states near the conduction band minimum (CBM) are localized on the AB′ stacking [Figs. 4(f) and 4(l)], whose size is also θ independent. This explains the experimentally observed large tunneling current at AB′ [27,28]. The distinct spatial localizations of electrons and holes originate from an in-plane strain-driven moiré potential [6]. For the unreconstructed lattice, the height of the moiré potential is identical at all AA′ stackings (≈132 meV). After lattice reconstruction, the height of the moiré potential at AA′ enclosed by the trimer is maximal (≈171 meV) and at other AA′ stackings is unmistakably smaller (≈98 meV) (Supplemental Material, Sec. V for details). The depth of the moiré potential at AB′ also changes after lattice reconstruction (≈ −306 meV with SR and ≈ −255 meV with SA, in meV). Furthermore, we have also obtained fully relaxed structures with SR and SA using DFT calculations for a $\sqrt{3} \times \sqrt{3} \times 1$ supercell of 58.47° $tBLMoS_2$. After applying a small ($s > 1.5\%$)compressive strain, we show that the lattice reconstructed structures obtained from SA are more stable (Supplemental Material, Sec. VI).

We have demonstrated reconstruction of the moiré lattices of TMDs for $\theta > 58.5°$. These structures can be probed using electron microscopy, optical imaging, etc., and are expected to be generic for tBLs with different sublattice atoms, including TMD heterostructures [17,27,28,45,52–60].

We thank the Supercomputer Education and Research Centre at IISc for providing computational resources, and Mit Naik, Shinjan Mandal, Sudipta Kundu for several useful discussions. H. R. K. thanks the Science and Engineering Research Board of the Department of Science and Technology, India for support under Grant No. SB/DF/005/2017.

[1] R. Bistritzer and A. H. MacDonald, Proc. Natl. Acad. Sci. **108**, 12233 (2011).

[2] Y. Cao, V. Fatemi, A. Demir, S. Fang, S. L. Tomarken, J. Y. Luo, J. D. Sanchez-Yamagishi, K. Watanabe, T. Taniguchi, E. Kaxiras, R. C. Ashoori, and P. Jarillo-Herrero, Nature (London) **556**, 80 (2018).

[3] Y. Cao, V. Fatemi, S. Fang, K. Watanabe, T. Taniguchi, E. Kaxiras, and P. Jarillo-Herrero, Nature (London) **556**, 43 (2018).

[4] M. Yankowitz, S. Chen, H. Polshyn, Y. Zhang, K. Watanabe, T. Taniguchi, D. Graf, A. F. Young, and C. R. Dean, Science **363**, 1059 (2019).

[5] M. H. Naik and M. Jain, Phys. Rev. Lett. **121**, 266401 (2018).
[6] M. H. Naik, S. Kundu, I. Maity, and M. Jain, Phys. Rev. B **102**, 075413 (2019).
[7] M. Fleischmann, R. Gupta, S. Sharma, and S. Shallcross, arXiv:1901.04679 (2019).
[8] L. Wang, E.-M. Shih, A. Ghiotto, L. Xian, D. A. Rhodes, C. Tan, M. Claassen, D. M. Kennes, Y. Bai, B. Kim, K. Watanabe, T. Taniguchi, X. Zhu, J. Hone, A. Rubio, A. N. Pasupathy, and C. R. Dean, Nat. Mater. **19**, 861 (2020).
[9] Z. Zhang, Y. Wang, K. Watanabe, T. Taniguchi, K. Ueno, E. Tutuc, and B. J. LeRoy, Nat. Phys. **16**, 1093 (2020).
[10] F. Wu, T. Lovorn, E. Tutuc, I. Martin, and A. H. MacDonald, Phys. Rev. Lett. **122**, 086402 (2019).
[11] Z. Bi, N. F. Q. Yuan, and L. Fu, Phys. Rev. B **100**, 035448 (2019).
[12] M. Angeli and A. H. MacDonald, arXiv:2008.01735 (2020).
[13] H. Pan, F. Wu, and S. Das Sarma, Phys. Rev. Research **2**, 033087 (2020).
[14] Z. Zhan, Y. Zhang, P. Lv, H. Zhong, G. Yu, F. Guinea, J. A. Silva-Guillén, and S. Yuan, Phys. Rev. B **102**, 241106(R) (2020).
[15] D. Zhai and W. Yao, Phys. Rev. Materials **4**, 094002 (2020).
[16] F. Gargiulo and O. V. Yazyev, 2D Materials **5**, 015019 (2017).
[17] H. Yoo, R. Engelke, S. Carr, S. Fang, K. Zhang, P. Cazeaux, S. H. Sung, R. Hovden, A. W. Tsen, T. Taniguchi, K. Watanabe, G.-C. Yi, M. Kim, M. Luskin, E. B. Tadmor, E. Kaxiras, and P. Kim, Nat. Mater. **18**, 448 (2019).
[18] P. Lucignano, D. Alfè, V. Cataudella, D. Ninno, and G. Cantele, Phys. Rev. B **99**, 195419 (2019).
[19] N. N. T. Nam and M. Koshino, Phys. Rev. B **96**, 075311 (2017).
[20] N. Leconte, S. Javvaji, J. An, and J. Jung, arXiv:1910.12805 (2019).
[21] D. Halbertal, N. R. Finney, S. S. Sunku, A. Kerelsky, C. Rubio-Verdú, S. Shabani, L. Xian, S. Carr, S. Chen, C. Zhang, L. Wang, D. Gonzalez-Acevedo, A. S. McLeod, D. Rhodes, K. Watanabe, T. Taniguchi, E. Kaxiras, C. R. Dean, J. C. Hone, A. N. Pasupathy, D. M. Kennes, A. Rubio, and D. N. Basov, Nat. Commun. **12**, 242 (2021).
[22] C. J. Pickard and R. J. Needs, J. Phys. Condens. Matter **23**, 053201 (2011).
[23] F. H. Stillinger, Phys. Rev. E **59**, 48 (1999).
[24] S. Kirkpatrick, C. D. Gelatt, and M. P. Vecchi, Science **220**, 671 (1983).
[25] S. Carr, D. Massatt, S. B. Torrisi, P. Cazeaux, M. Luskin, and E. Kaxiras, Phys. Rev. B **98**, 224102 (2018).
[26] V. V. Enaldiev, V. Zólyomi, C. Yelgel, S. J. Magorrian, and V. I. Fal'ko, Phys. Rev. Lett. **124**, 206101 (2020).
[27] A. Weston, Y. Zou, V. Enaldiev, A. Summerfield, N. Clark, V. Zólyomi, A. Graham, C. Yelgel, S. Magorrian, M. Zhou, J. Zultak, D. Hopkinson, A. Barinov, T. H. Bointon, A. Kretinin, N. R. Wilson, P. H. Beton, V. I. Fal'ko, S. J. Haigh, and R. Gorbachev, Nat. Nanotechnol. **15**, 592 (2020).
[28] M. R. Rosenberger, H.-J. Chuang, M. Phillips, V. P. Oleshko, K. M. McCreary, S. V. Sivaram, C. S. Hellberg, and B. T. Jonker, ACS Nano **14**, 4550 (2020).
[29] See Supplemental Material at http://link.aps.org/supplemental/10.1103/PhysRevB.103.L121102 for simulation details, reconstruction of other TMDs, several transient structures, confining moiré potential computed with DFT, and structural relaxation with DFT.
[30] S. Plimpton, J. Comput. Phys. **117**, 1 (1995).
[31] E. Bitzek, P. Koskinen, F. Gähler, M. Moseler, and P. Gumbsch, Phys. Rev. Lett. **97**, 170201 (2006).
[32] J.-W. Jiang and Y.-P. Zhou, *Handbook of Stillinger-Weber Potential Parameters for Two-Dimensional Atomic Crystals* (InTechOpen, 2017).
[33] M. H. Naik, I. Maity, P. K. Maiti, and M. Jain, J. Phys. Chem. C **123**, 9770 (2019).
[34] A. Togo and I. Tanaka, Scr. Mater. **108**, 1 (2015).
[35] W. Kohn and L. J. Sham, Phys. Rev. **140**, A1133 (1965).
[36] L. Lin, A. García, G. Huhs, and C. Yang, J. Phys.: Condens. Matter **26**, 305503 (2014).
[37] J. M. Soler, E. Artacho, J. D. Gale, A. García, J. Junquera, P. Ordejón, and D. Sánchez-Portal, J. Phys.: Condens. Matter **14**, 2745 (2002).
[38] V. W. zhe Yu, F. Corsetti, A. García, W. P. Huhn, M. Jacquelin, W. Jia, B. Lange, L. Lin, J. Lu, W. Mi, A. Seifitokaldani, Álvaro Vázquez-Mayagoitia, C. Yang, H. Yang, and V. Blum, Comput. Phys. Commun. **222**, 267 (2018).
[39] R. Car, W. E, L. Lin, J. Lu, and L. Ying, Commun. Math. Sci. **7**, 755 (2009).
[40] N. Troullier and J. L. Martins, Phys. Rev. B **43**, 1993 (1991).
[41] M. Dion, H. Rydberg, E. Schröder, D. C. Langreth, and B. I. Lundqvist, Phys. Rev. Lett. **92**, 246401 (2004).
[42] V. R. Cooper, Phys. Rev. B **81**, 161104(R) (2010).
[43] M. van Setten, M. Giantomassi, E. Bousquet, M. Verstraete, D. Hamann, X. Gonze, and G.-M. Rignanese, Comput. Phys. Commun. **226**, 39 (2018).
[44] L. Liang, A. A. Puretzky, B. G. Sumpter, and V. Meunier, Nanoscale **9**, 15340 (2017).
[45] J. S. Alden, A. W. Tsen, P. Y. Huang, R. Hovden, L. Brown, J. Park, D. A. Muller, and P. L. McEuen, Proc. Natl. Acad. Sci. **110**, 11256 (2013).
[46] C. D. Modes and R. D. Kamien, Soft Matter **9**, 11078 (2013).
[47] I. Maity, P. K. Maiti, and M. Jain, Phys. Rev. B **97**, 161406(R) (2018).
[48] K. Zhang and E. B. Tadmor, J. Mech. Phys. Solids **112**, 225 (2018).
[49] I. Maity, M. H. Naik, P. K. Maiti, H. R. Krishnamurthy, and M. Jain, Phys. Rev. Research **2**, 013335 (2020).
[50] K. Sun, A. Souslov, X. Mao, and T. C. Lubensky, Proc. Natl. Acad. Sci. **109**, 12369 (2012).
[51] T. Riste, *Ordering in Strongly Fluctuating Condensed Matter Systems* (Springer Science & Business Media, 2012), Vol. 50.
[52] C. Zhang, M.-Y. Li, J. Tersoff, Y. Han, Y. Su, L.-J. Li, D. A. Muller, and C.-K. Shih, Nat. Nanotechnol. **13**, 152 (2018).
[53] Y. Xu, S. Liu, D. A. Rhodes, K. Watanabe, T. Taniguchi, J. Hone, V. Elser, K. F. Mak, and J. Shan, Nature (London) **587**, 214 (2020).
[54] T. I. Andersen, G. Scuri, A. Sushko, K. De Greve, J. Sung, Y. Zhou, D. S. Wild, R. J. Gelly, H. Heo, D. Bérubé, A. Y. Joe, L. A. Jauregui, K. Watanabe, T. Taniguchi, P. Kim, H. Park, and M. D. Lukin, Nat. Mater. (2021).
[55] G. Scuri, T. I. Andersen, Y. Zhou, D. S. Wild, J. Sung, R. J. Gelly, D. Bérubé, H. Heo, L. Shao, A. Y. Joe, A. M. Mier Valdivia, T. Taniguchi, K. Watanabe, M. Lončar, P. Kim, M. D. Lukin, and H. Park, Phys. Rev. Lett. **124**, 217403 (2020).

[56] H. Baek, M. Brotons-Gisbert, Z. X. Koong, A. Campbell, M. Rambach, K. Watanabe, T. Taniguchi, and B. D. Gerardot, Sci. Adv. **6**, eaba8526 (2020).

[57] G. X. Ni, H. Wang, B.-Y. Jiang, L. X. Chen, Y. Du, Z. Y. Sun, M. D. Goldflam, A. J. Frenzel, X. M. Xie, M. M. Fogler, and D. N. Basov, Nat. Commun. **10**, 4360 (2019).

[58] L. Jiang, Z. Shi, B. Zeng, S. Wang, J.-H. Kang, T. Joshi, C. Jin, L. Ju, J. Kim, T. Lyu, Y.-R. Shen, M. Crommie, H.-J. Gao, and F. Wang, Nat. Mater. **15**, 840 (2016).

[59] J. Holler, S. Meier, M. Kempf, P. Nagler, K. Watanabe, T. Taniguchi, T. Korn, and C. Schüller, Appl. Phys. Lett. **117**, 013104 (2020).

[60] A. C. Gadelha, D. A. A. Ohlberg, C. Rabelo, E. G. S. Neto, T. L. Vasconcelos, J. L. Campos, J. S. Lemos, V. Ornelas, D. Miranda, R. Nadas, F. C. Santana, K. Watanabe, T. Taniguchi, B. van Troeye, M. Lamparski, V. Meunier, V.-H. Nguyen, D. Paszko, J.-C. Charlier, L. C. Campos, L. G. Cançado, G. Medeiros-Ribeiro, and A. Jorio, arXiv:2006.09482 (2020).